
A Latent Neural ODE-VAE for Modeling Hippocampal Population Activity on Low-Dimensional Manifolds

Anonymous Author(s)

Affiliation

Address

email

Abstract

1 Neural population activity traces trajectories in a high-dimensional state space, yet
2 accumulating evidence suggests these trajectories are confined to low-dimensional
3 manifolds that encode both task variables and internal state. Existing manifold
4 inference pipelines can recover geometry and explain variability, but often rely on
5 multi-stage local models and do not impose globally smooth continuous-time dy-
6 namics. We develop a latent Neural ODE variational autoencoder (ODE-VAE) that
7 jointly learns (i) a low-dimensional stochastic initial condition, (ii) continuous-time
8 latent dynamics parameterized by a mixture-of-experts ODE, and (iii) a decoder
9 back to neural activity. To better align reconstruction with temporally structured
10 variability, our v5 implementation adds transition-consistency regularization in ob-
11 servation space and a soft locally linear embedding (LLE) constraint in latent space.
12 On synthetic random-foraging sequences, the model achieves high reconstruction
13 accuracy ($R^2 = 0.9789$) while exhibiting seed sensitivity. On the E65 hippocampal
14 calcium dataset, the latest v5 baseline run attains final PCA-space reconstruction
15 $R^2 = 0.4506$ (best epoch $R^2 = 0.4785$), but performance varies substantially with
16 preprocessing, split strategy, and evaluation space. Together, these results highlight
17 both the promise and current fragility of end-to-end continuous-time manifold
18 models for noisy biological recordings.

19

1 Introduction

20 Neural activity can be described as a point in a high-dimensional coordinate system, where each
21 coordinate axis represents a single neuron's activity [Cunningham and Yu, 2014]. Underlying
22 properties of the network and its inputs can confine neural trajectories to a subregion of this space,
23 often referred to as a neural manifold [Cunningham and Yu, 2014, Gallego et al., 2017]. The
24 neural manifold has been proposed to underlie motor movements [Gallego et al., 2017, Russo et al.,
25 2018], head direction cells [Chaudhuri et al., 2019], and hippocampal maps of physical variables
26 [O'Keefe and Dostrovsky, 1971, Frank et al., 2000, Wood et al., 2000, O'Keefe and Nadel, 1978].
27 The conceptual ideas in these studies suggest a general principle of hippocampal computation: the
28 construction of organized maps of learned knowledge instantiated by neural manifolds [Tolman, 1948,
29 O'Keefe and Nadel, 1978, Stachenfeld et al., 2017, Bellmund et al., 2018, Nieh et al., 2021].

30 Nonlinear dimensionality reduction has demonstrated that neural population activity can often be
31 described by 4–6 latent variables, suggesting that activity is constrained to a low-dimensional neural
32 manifold that displays a geometric representation of both physical and abstract variables [Low
33 et al., 2018, Chaudhuri et al., 2019, Nieh et al., 2021]. Existing approaches are limited to multi-
34 stage machine-learning pipelines, using forest-based transition models (with probabilistic principal
35 component analysis in decision-tree leaves) to define distances between population states, which are
36 then embedded into a low-dimensional manifold and mapped back to neural activity for reconstruction

[Low et al., 2018, Tipping and Bishop, 1999, Breiman, 2001, Tenenbaum et al., 2000, Yu et al., 2009]. This piecewise approach partitions state space and models dynamics locally, hence lacking explicit enforcement of globally smooth latent dynamics and can exhibit saturation of reconstruction decoding performance with low-dimensional embeddings [Low et al., 2018]. Thus, we hypothesize that generative deep learning models offer a complementary framework: neural network architectures can be trained directly on biological neural population recordings to jointly learn low-dimensional latent coordinates, their temporal evolution, and the mapping back to neural activity [Kingma and Welling, 2014, Chen et al., 2018, Rubanova et al., 2019].

In this paper, we propose a novel approach to modeling the neural manifold by constructing a Neural Ordinary Differential Equation variational autoencoder (ODE-VAE): a deep generative model that (i) encodes high-dimensional population activity into a low-dimensional latent state, (ii) models the evolution of that latent state as a continuous-time dynamical system parameterized by a neural ODE, and (iii) decodes the resulting latent trajectory back into neural activity [Kingma and Welling, 2014, Chen et al., 2018, Rubanova et al., 2019]. By training the encoder, dynamics, and decoder end-to-end under a variational objective, this approach aims to capture nonlinear manifold structure while imposing smooth temporal dynamics. Our v5 implementation introduces mixture-of-experts latent dynamics and adds two regularizers inspired by manifold inference—transition-consistency in observation space and a soft locally linear embedding (LLE) constraint in latent space [Low et al., 2018, Saul and Roweis, 2003]. We evaluate this family on synthetic and hippocampal calcium datasets and analyze the sensitivity of performance to preprocessing and evaluation choices.

Contributions.

- We formalize an ODE-VAE for trialized population sequences with mixture-of-experts latent dynamics and explicit geometric regularizers.
- We instantiate this formulation in a versioned codebase (v1–v6) and present v5 as the primary model with transition and soft-LLE regularization.
- We provide a reproducible evaluation on synthetic and hippocampal calcium datasets and identify protocol factors that strongly affect reconstruction metrics.

Related Work

Our approach lies at the intersection of manifold-based neuroscience and latent dynamical systems. In hippocampus, the cognitive map framework and subsequent experimental work motivate geometric organization of population codes [Tolman, 1948, O’Keefe and Dostrovsky, 1971, O’Keefe and Nadel, 1978, Eichenbaum and Cohen, 2014], including abstract and non-spatial representations [Aronov et al., 2017, Tavares et al., 2015, Constantinescu et al., 2016, Schuck and Niv, 2019, Park et al., 2020, Nieh et al., 2021]. Beyond classical place coding, hippocampal population activity reflects trajectory and sequential organization [Frank et al., 2000, Pastalkova et al., 2008, MacDonald et al., 2011, Taxidis et al., 2020], episodic variables at shared locations [Wood et al., 2000, Gill et al., 2011, McKenzie et al., 2014], and multimodal/task variables such as odor and taste [Eichenbaum et al., 1987, Herzog et al., 2019]. Manifold inference methods can recover low-dimensional structure and explain structured variability beyond measured task variables [Low et al., 2018, Chaudhuri et al., 2019, Rubin et al., 2019].

In machine learning, variational autoencoders [Kingma and Welling, 2014] and neural ODEs [Chen et al., 2018] provide a principled framework for continuous-time latent-variable modeling. Latent ODEs extend this idea to irregularly sampled sequences [Rubanova et al., 2019]. We adopt this framework but tailor the encoder, evaluation protocol, and regularization to the neuroscience setting, emphasizing trialized sequences, explicit geometric constraints, and comparisons to MIND-style evaluation pipelines [Low et al., 2018]. For calcium imaging recordings, related methodological work has emphasized motion correction and demixing/denoising [Pnevmatikakis et al., 2016, Pnevmatikakis and Giovannucci, 2017], highlighting the importance of preprocessing choices when evaluating reconstruction metrics.

86 **3 Problem Setup and Data**

87 We study trialized population activity sequences. Let $y_b(t_\ell) \in \mathbb{R}^N$ denote the raw activity of
 88 N simultaneously recorded units/ROIs on trial $b \in \{1, \dots, B\}$ at resampled time t_ℓ , where $\ell \in$
 89 $\{1, \dots, L\}$ indexes a fixed-length grid. We write $Y_b \in \mathbb{R}^{L \times N}$ for the stacked sequence.

90 **Observation space.** In v5, the model is trained on a PCA-projected representation of activity.
 91 Let $x_b(t_\ell) \in \mathbb{R}^K$ be the K -dimensional PCA coordinate at time t_ℓ , and let $X_b \in \mathbb{R}^{L \times K}$ be the
 92 corresponding trial sequence. Unless otherwise stated, all losses and reported R^2 values for v5 are
 93 computed in this PCA space. For some evaluations (e.g., the optional sweep path), reconstructions
 94 are mapped back to raw ROI space via inverse PCA and de-normalization.

95 **Time grid.** Trials are resampled to a common duration and the time vector is normalized to $[0, 1]$;
 96 we denote the resulting grid by $0 = t_1 < \dots < t_L = 1$. The latent dimension is denoted by D .

97 **E65 dataset.** We use the Schottorf Lab E65 dataset (E65_data.npz), containing calcium activity
 98 ($\Delta F/F$) from $N = 375$ ROIs over $T = 7434$ frames, along with trial IDs, timestamps, and aligned
 99 behavioral covariates. In the v5 preprocessing path: (i) PCA is fit to the full recording and retains
 100 95% variance, producing $K = 129$ components; (ii) frames are grouped by trial, the first 10 trials
 101 are dropped, and each trial is linearly interpolated to a fixed length $L = 120$ (trial_len_s=12,
 102 fps=10); (iii) the time vector is normalized to $[0, 1]$; (iv) each PCA component is standardized over
 103 time (session-level z-score) and an optional per-trial baseline is removed by subtracting the mean of
 104 the first 5 resampled bins. After filtering, 180 trials are available; default validation holds out the
 105 last 3 trials (train 177 / val 3). For efficiency, the default configuration further subsamples to 100
 106 sequences via greedy landmark selection.

107 **Synthetic benchmark.** We additionally evaluate on synthetic_rat_data.npz (4000 frames,
 108 300 neurons, 20 trials), which provides a controlled benchmark for recoverability of smooth low-
 109 dimensional dynamics.

110 **4 Model: Latent Neural ODE-VAE**

111 **4.1 Stochastic encoder**

112 For each trial, the encoder uses only $x_b(t_1)$ and outputs a diagonal Gaussian posterior on the latent
 113 initial state:

$$q_\phi(z_{0,b} | x_b(t_1)) = \mathcal{N}(\mu_b, \text{diag}(\sigma_b^2)), \quad (1)$$

114 with reparameterization

$$z_{0,b} = \mu_b + \sigma_b \odot \epsilon, \quad \epsilon \sim \mathcal{N}(0, I). \quad (2)$$

115 Here $z_{0,b} \in \mathbb{R}^D$, $\mu_b \in \mathbb{R}^D$, $\sigma_b \in \mathbb{R}_{>0}^D$, and \odot denotes elementwise multiplication.

116 **4.2 Continuous-time latent dynamics**

117 Latent trajectories are generated by a neural ODE:

$$\frac{dz_b(t)}{dt} = f_\theta(z_b(t), t), \quad z_b(t_1) = z_{0,b}. \quad (3)$$

118 In v5, f_θ is a mixture of experts:

$$f_\theta(z, t) = \sum_{e=1}^E \pi_e(z) f_e(z), \quad \pi(z) = \text{softmax}(g(z)), \quad (4)$$

119 with $E = 4$ latent experts by default and Dormand–Prince integration (dopri5). Each expert
 120 $f_e : \mathbb{R}^D \rightarrow \mathbb{R}^D$ is an MLP and $\pi_e(z) \in [0, 1]$ are gating weights satisfying $\sum_e \pi_e(z) = 1$.

121 **4.3 Decoder family**

122 A decoder maps latent states back to observations:

$$\hat{x}_b(t_\ell) = g_\psi(z_b(t_\ell)). \quad (5)$$

123 The codebase supports MLP, neuron-aware, local-attention, and MoE decoders; v5 default is MoE
 124 decoder with 8 decoder experts. In all cases, $g_\psi : \mathbb{R}^D \rightarrow \mathbb{R}^K$ outputs the mean of a factorized
 125 Gaussian observation model in PCA space.

126 **5 Training Objective and Regularization**

127 We optimize a variational objective with auxiliary regularizers. Under a Gaussian observation model
 128 $p_\psi(x_b(t_\ell) | z_b(t_\ell)) = \mathcal{N}(g_\psi(z_b(t_\ell)), \sigma^2 I)$ with fixed σ^2 , maximizing the ELBO corresponds (up to
 129 constants and a scale factor) to minimizing mean-squared reconstruction error plus a KL penalty.

130 The base objective combines reconstruction and KL terms:

$$\mathcal{L}_{\text{base}} = \mathcal{L}_{\text{rec}} + \beta \mathcal{L}_{\text{KL}}, \quad (6)$$

131 where

$$\mathcal{L}_{\text{rec}} = \frac{1}{B L K} \sum_{b=1}^B \sum_{\ell=1}^L \|\hat{x}_b(t_\ell) - x_b(t_\ell)\|_2^2, \quad (7)$$

$$\mathcal{L}_{\text{KL}} = \frac{1}{B} \sum_b D_{\text{KL}}(q_\phi(z_{0,b} | x_b(t_1)) \| \mathcal{N}(0, I)). \quad (8)$$

133 Equivalently, the (negative) ELBO per trial is

$$\mathcal{L}_{\text{ELBO}} = -\mathbb{E}_{q_\phi(z_{0,b} | x_b(t_1))} \left[\sum_{\ell=1}^L \log p_\psi(x_b(t_\ell) | z_b(t_\ell)) \right] + \beta D_{\text{KL}}(q_\phi(z_{0,b} | x_b(t_1)) \| p(z_{0,b})), \quad (9)$$

134 with prior $p(z_{0,b}) = \mathcal{N}(0, I)$. In practice, the code uses a single Monte Carlo sample of $z_{0,b}$ per trial
 135 and minibatch.

Smoothness regularization.

$$\mathcal{L}_{\text{smooth}} = \frac{1}{B(L-1)D} \sum_{b,\ell} \left\| \frac{z_b(t_{\ell+1}) - z_b(t_\ell)}{t_{\ell+1} - t_\ell} \right\|_2^2. \quad (10)$$

Transition-aware regularization (v5).

$$\mathcal{L}_{\text{trans}} = \frac{1}{B(L-1)K} \sum_{b,\ell} \left\| (\hat{x}_b(t_{\ell+1}) - \hat{x}_b(t_\ell)) - (x_b(t_{\ell+1}) - x_b(t_\ell)) \right\|_2^2. \quad (11)$$

136 This term is linearly warmed up for the first 30 epochs.

137 **Soft LLE latent regularization (v5).** For flattened latent points $\{z_i\}_{i=1}^M \subset \mathbb{R}^D$, with k -NN set
 138 $\mathcal{N}_k(i)$, we add a soft locally linear embedding penalty [Saul and Roweis, 2003]:

$$\mathcal{L}_{\text{LLE}} = \frac{1}{M} \sum_{i=1}^M \left\| z_i - \sum_{j \in \mathcal{N}_k(i)} w_{ij} z_j \right\|_2^2, \quad w_{ij} \propto \exp\left(-\frac{\|z_i - z_j\|_2}{\tau}\right). \quad (12)$$

139 Default parameters: $k = 8$, $M \leq 256$, $\tau = 0.1$.

Total loss.

$$\mathcal{L} = \mathcal{L}_{\text{rec}} + \beta_t \mathcal{L}_{\text{KL}} + \lambda_{\text{smooth}} \mathcal{L}_{\text{smooth}} + \lambda_{\text{trans},t} \mathcal{L}_{\text{trans}} + \lambda_{\text{LLE}} \mathcal{L}_{\text{LLE}}. \quad (13)$$

140 The KL coefficient β_t is warmed up over 30 epochs to a final value $\beta = 0.02$.

141 6 Versioned Model Development and Failure Modes

142 The repository contains a sequence of incrementally modified training scripts that reflect both
143 model and pipeline iteration: the current implementation is `v5_neural_vae.py` and earlier variants
144 are archived under `neuroscience/src/archived_ode_models/`. These versions should not be
145 interpreted as a clean ablation study: they differ in architecture, preprocessing, evaluation space,
146 solver choices, and logging conventions. Nevertheless, documenting this evolution is useful for
147 understanding observed fragilities and for motivating the v5 regularizers, which are directly inspired
148 by the geometry- and transition-aware components of the MIND pipeline [Low et al., 2018, Saul and
149 Roweis, 2003].

150 **v1: baseline latent Neural ODE-VAE.** v1 implements the minimal continuous-time VAE setup
151 [Kingma and Welling, 2014, Chen et al., 2018]: an MLP encoder of $x(t_1)$, a single latent vector
152 field f_θ , an MLP decoder, and an ℓ_2 smoothness penalty on finite-difference latent velocities. It also
153 introduces global PCA preprocessing and greedy landmark selection, mirroring common manifold
154 inference practice [Low et al., 2018]. *Vulnerabilities:* (i) PCA is fit on the full recording before
155 the train/val split, which can leak test-set structure into the representation; (ii) landmark selection
156 is performed on flattened time points and mapped back to trials via a modulo operation, which
157 can duplicate trials and bias the subsample away from true trial-level coverage; (iii) the default
158 “last- K trials” holdout is sensitive to nonstationarities or ordering effects. *Motivation for v2:* reduce
159 protocol-induced optimism by splitting first and fitting normalization/PCA only on training data, and
160 explore more expressive dynamics.

161 **v2: switching/gated latent dynamics with train-only preprocessing.** v2 adds a learned gating
162 network over multiple candidate latent vector fields (a switching/mixture-style dynamics), increasing
163 expressivity beyond a single global f_θ . Crucially, v2 builds raw trial sequences first, then performs
164 the train/val split, and fits both standardization and PCA on training data only; evaluation reconstructs
165 back to raw ROI space via inverse PCA before scoring, which is closer to MIND-style reporting
166 [Low et al., 2018]. *Vulnerabilities:* (i) time normalization to $[0, 1]$ is disabled in the script, which
167 changes the effective scale seen by the ODE solver and can make optimization more sensitive; (ii)
168 gating dynamics introduce additional nonconvexity and can collapse to a single expert without careful
169 tuning. *Motivation for v3:* incorporate mixture-of-experts dynamics and richer decoders to better
170 capture heterogeneous neural tuning and trial-to-trial variability.

171 **v3: mixture-of-experts latent ODE and decoder variants.** v3 introduces a mixture-of-experts
172 latent vector field (soft gating over multiple f_e) and a family of decoders (neuron-aware, local-
173 attention, and MoE decoders) intended to better model neuron-specific heterogeneity. It also adds
174 an optional per-trial baseline correction (subtracting early-bin means) to reduce drift/offset burden
175 on the latent state. *Vulnerabilities:* (i) the preprocessing/evaluation pipeline reverts to full-session
176 PCA and PCA-space scoring, making results harder to compare to raw-space metrics and potentially
177 optimistic; (ii) the flattened-time landmark subsampling and last- K holdout issues from v1 persist;
178 (iii) added model capacity increases overfitting risk when validation is extremely small. *Motivation*
179 *for v4:* refine the decoder locality bias and improve hardware compatibility (notably Apple MPS)
180 while keeping the MoE latent dynamics.

181 **v4: MoE latent dynamics with locality-biased decoders (MPS-safe).** v4 largely preserves v3’s
182 MoE latent dynamics and decoder choices, and emphasizes MPS-safe ODE integration (fixed-step
183 fallbacks) to reduce device-specific solver failures during experimentation. *Vulnerabilities:* decoder
184 “locality” is primarily architectural (attention-like) rather than enforced by an explicit geometric
185 objective, and the pipeline-level issues (PCA leakage, trial subsampling bias, small/ordered holdout)
186 remain. *Motivation for v5:* add explicit constraints that directly regularize temporal transitions and
187 local manifold geometry, closer in spirit to MIND’s use of transition structure and neighborhood
188 geometry [Low et al., 2018, Saul and Roweis, 2003].

189 **v5: transition consistency + soft-LLE geometry regularization.** The current v5 model retains
190 MoE latent dynamics and MoE decoding while adding two explicit regularizers: (i) a transition-
191 consistency loss in observation space that matches $\Delta\hat{x}(t)$ to $\Delta x(t)$ and (ii) a soft LLE penalty that
192 encourages each latent point to be reconstructible from its k -NN neighborhood [Saul and Roweis,

193 Both are motivated by the observation that reconstruction alone can ignore fine-grained temporal
 194 and local geometric structure, which MIND leverages via transition-aware distances and local
 195 mappings [Low et al., 2018]. *Vulnerabilities*: (i) the default training script still subsamples training
 196 data using flattened-time landmark selection and uses a small ordered validation set, amplifying
 197 sensitivity to preprocessing and random seed; (ii) the codebase supports multiple evaluation spaces
 198 (PCA vs raw), so reported R^2 values are not directly comparable unless the evaluation definition
 199 is matched; (iii) the v5 checkpoint-saving logic contains a minor best-model saving bug (the “best”
 200 condition is checked again after updating the best value), which can prevent true best checkpoints
 201 from being written and complicate retrospective comparisons. *Motivation for v6*: test whether
 202 PCA-space training masks raw-space reconstruction error by training and scoring directly in raw
 203 neuron space.

204 **v6: no-PCA, raw-space variant.** v6 is a v5-style variant that bypasses PCA and optimizes
 205 reconstruction directly in the original ROI space. This makes the metric closer to the scientific
 206 target and avoids ambiguity about the evaluation space. *Vulnerabilities*: raw-space optimization is
 207 substantially higher-dimensional and noisier, which can reduce stability and yield lower R^2 without
 208 additional noise modeling or stronger inductive biases; it also makes comparisons to PCA-trained
 209 runs nontrivial unless preprocessing is standardized.

210 7 Experimental Protocol

211 7.1 Configurations

212 Main v5 settings from config.txt: latent dimension $D = 5$ (with a sweep to $D = 8$), batch size 8,
 213 150 epochs, Adam optimizer (learning rate 0.002, weight decay 10^{-5}), $\lambda_{\text{smooth}} \in \{5 \times 10^{-4}, 2 \times 10^{-4}\}$,
 214 $\lambda_{\text{trans}} = 0.01$ with a 30-epoch warmup, $\lambda_{\text{LLE}} = 0.01$, landmark count 100, and baseline correction
 215 enabled.

216 **Implementation details.** The encoder is an MLP with hidden widths 512–256–128. The latent
 217 vector field uses $E = 4$ experts with hidden width 128 and a learned gating network; derivatives
 218 are layer-normalized for stability. For reconstruction, the default v5 decoder is a mixture-of-experts
 219 network with 8 decoder experts and hidden width 256. Latent dynamics are integrated with Dormand–
 220 Prince (dopri5) using tolerances `rtol=1e-3` and `atol=1e-4`. Gradients are clipped to max norm
 221 1.0.

222 7.2 Metrics

223 The primary training metric is coefficient of determination,

$$R^2 = 1 - \frac{\sum_{b,\ell} \|x_b(t_\ell) - \hat{x}_b(t_\ell)\|_2^2}{\sum_{b,\ell} \|x_b(t_\ell) - \bar{x}\|_2^2}, \quad (14)$$

224 where $\bar{x} = \frac{1}{BL} \sum_{b,\ell} x_b(t_\ell)$ denotes the mean activity vector across all validation entries in the
 225 evaluation space. Our implementation supports two evaluation styles: (i) PCA-space R^2 and (ii) strict
 226 raw-neuron-space R^2 via inverse PCA and de-normalization. We report values as saved in the run
 227 metadata for each experiment.

228 8 Results

229 8.1 Synthetic benchmark: high ceiling with seed sensitivity

230 Table 1 summarizes a five-seed sweep on synthetic data. The best seed reaches $R^2 = 0.9789$.
 231 Excluding the divergent run, the mean performance is $R^2 = 0.828 \pm 0.141$ (std. dev.), indicating
 232 sensitivity to initialization even in a controlled setting.

233 8.2 E65 hippocampal data: mixed performance across variants

234 Table 2 reports available E65 run metrics for the ODE-VAE family. The most recent run in the
 235 repository (2026-02-20_172318_6880b5b) achieves a final PCA-space $R^2 = 0.4506$ with best-

Table 1: Synthetic random-foraging benchmark from `seed_sweep_results.txt`.

Seed	Final R^2	Best validation loss
1	0.9789	0.06642
42	0.6757	0.40521
1337	0.9116	0.16298
2025	0.7467	0.31145
777	0.0000 (NaN collapse)	∞
Mean (all seeds)	0.6626	—
Mean (non-collapsed seeds)	0.8282	—

Table 2: E65 reconstruction metrics extracted from saved run artifacts. Sweep runs report both best-epoch and final R^2 as logged during training.

Variant	Space	D	λ_{smooth}	Best R^2	Final R^2
latest v5 baseline	PCA	5	5×10^{-4}	0.4785	0.4506
archived ODE-VAE	PCA	—	—	—	0.4368
v5 sweep	PCA	5	5×10^{-4}	0.0354	-0.2391
v5 sweep	PCA	5	2×10^{-4}	0.0353	-0.1382
v5 sweep	PCA	8	5×10^{-4}	0.0569	-0.2022
v6 (no PCA)	raw	—	—	—	0.0956

epoch $R^2 = 0.4785$. An earlier archived ODE-VAE run reports $R^2 = 0.4368$. In contrast, v5 sweep artifacts are substantially lower (best-epoch $R^2 \leq 0.0569$, negative final R^2 in three runs), while a no-PCA v6 run records $R^2 = 0.0956$. These discrepancies are consistent with the codebase supporting multiple evaluation spaces and split protocols; therefore, comparisons across runs should be interpreted cautiously unless the evaluation definition is matched.

8.3 Manifold interpretability

The codebase saves latent manifold projections (MDS) and reconstruction diagnostics for each run. Figure 1 shows an example latent trajectory embedding from the trained model artifacts.

9 Discussion

The model captures the intended inductive bias: low-dimensional continuous latent trajectories with explicit geometric regularization. On synthetic data, this bias is highly effective. On real E65 recordings, however, results are sensitive to implementation and evaluation choices.

Three factors emerge from the saved run artifacts:

1. **Metric-space mismatch.** PCA-space training can look favorable while strict raw-space R^2 may degrade. This is particularly salient when comparing to MIND-style evaluations, which reconstruct back to neuron space (via inverse PCA) before scoring [Low et al., 2018].
2. **Data-efficiency tradeoff.** Landmark subsampling (100 selected sequences from 180 usable trials) accelerates training but may reduce generalization. In MIND, landmarks primarily support graph construction and embedding; the learned mapping is then applied to all eligible time points [Low et al., 2018].
3. **Optimization stability.** Strong regularization with small validation sets (3 trials) and stiff latent dynamics can produce unstable or negative final R^2 , despite early high points.

These observations suggest that future gains likely require protocol-level changes in addition to architectural changes: larger and randomized holdout splits, early stopping on a stable cross-validated objective, trial-level (not frame-level) landmark selection, and direct raw-space reconstruction losses.

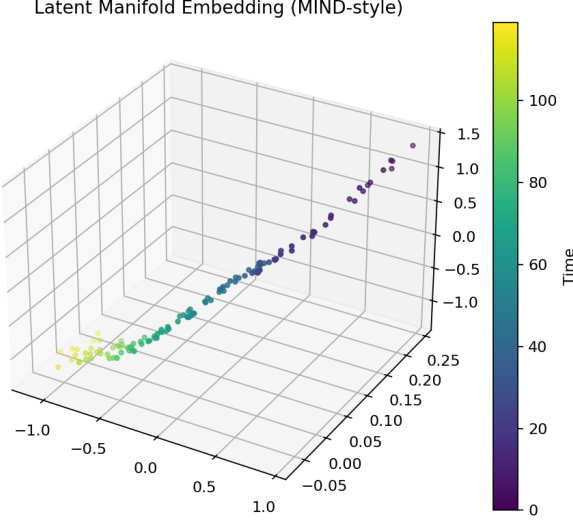


Figure 1: Latent manifold embedding produced by the ODE-VAE analysis pipeline.

261 10 Future Work

262 A central motivation of this project is to connect end-to-end continuous-time latent dynamical
 263 modeling with the multi-stage manifold inference pipeline used in MIND [Low et al., 2018]. Our
 264 current codebase already adopts several MIND-inspired components (global PCA preprocessing,
 265 greedy landmark selection for visualization, and MDS-based manifold plots), but the modeling
 266 philosophy differs: MIND estimates a graph of transition structure via a PPCA regression forest and
 267 learns explicit local mappings between ambient activity and manifold coordinates [Low et al., 2018,
 268 Tipping and Bishop, 1999, Breiman, 2001], whereas the ODE-VAE learns a single global generative
 269 model (encoder + latent dynamics + decoder) by optimizing a reconstruction objective [Kingma and
 270 Welling, 2014, Chen et al., 2018, Rubanova et al., 2019]. Below we outline concrete directions to
 271 tighten this connection and improve robustness on calcium recordings.

272 10.1 Match MIND-style evaluation protocols and metrics

273 Many apparent discrepancies across saved E65 runs are consistent with evaluation-definition mis-
 274 match. In the MIND Matlab cross-validation script, trials are split randomly (e.g., 90/10), reconstruc-
 275 tion is scored in the original neuron space after mapping back through inverse PCA, and performance
 276 is visualized both as an overall score and as per-trial dots [Low et al., 2018]. Aligning our training and
 277 reporting with this protocol would make comparisons substantially more interpretable. Concretely,
 278 we plan to (i) report both Pearson correlation on vectorized activity blocks,

$$r = \text{corr}\left(\text{vec}(Y_{\text{test}}), \text{vec}(\hat{Y}_{\text{test}})\right), \quad (15)$$

279 and variance-explained R^2 under repeated random trial splits, and (ii) include held-out neuron
 280 evaluation where latents are inferred from a subset of neurons and used to predict excluded neurons,
 281 mirroring the “cell prediction” analyses in MIND [Low et al., 2018]. This will also require revisiting
 282 the current practice of validating on the final 3 trials, which can conflate generalization with drift.

283 10.2 Use landmarks for geometry, not for shrinking the training set

284 In MIND, landmarks are an efficiency device for graph construction and embedding; the learned
 285 mapping is then applied to all eligible time points [Low et al., 2018]. In contrast, the default v5
 286 configuration further subsamples the dataset down to 100 landmarked sequences (from 180 trials),
 287 which likely increases estimator variance and can bias which trials are emphasized during training.
 288 A straightforward next step is to train the ODE-VAE on all trials/time points and reserve landmark
 289 selection for: (i) visualization, (ii) neighbor graph construction for local regularizers, and (iii)

290 lightweight geometric diagnostics (e.g., random-walk distance embeddings). This change should
291 directly improve stability without changing the model class.

292 **10.3 Hybrid decoders: combine global reconstruction with MIND-like local mappings**

293 The MIND pipeline learns mappings between ambient PCA space and manifold coordinates using
294 locally weighted methods (e.g., LLE regression) [Saul and Roweis, 2003, Low et al., 2018]. This
295 provides a natural mechanism to capture sharp, local irregularities that global regressors may smooth
296 out. Our current v5 decoders are global function approximators (MLP/MoE), which can yield good
297 coarse reconstructions but may miss neuron-specific transients. An appealing hybrid is a global
298 decoder plus a local residual term defined over nearby latent states,

$$\hat{x}(t) = g_\psi(z(t)) + \sum_{j \in \mathcal{N}_k(z(t))} \alpha_j(z(t)) r_j, \quad (16)$$

299 where $\mathcal{N}_k(\cdot)$ are neighbors in latent space (or in a MIND-style random-walk metric), $r_j \in \mathbb{R}^K$ are
300 learned prototype residuals, and α_j are normalized weights (e.g., softmax over distances). This would
301 preserve the interpretability and global smoothness of the ODE while injecting the kind of local
302 adaptivity that MIND’s mapping stage provides.

303 **10.4 Optimize and score in raw neuron space (with PCA as an internal linear layer)**

304 Several E65 runs in this repository train and score in different spaces (PCA vs raw ROI), making R^2
305 values hard to compare. MIND keeps PCA primarily as a compression step but reconstructs back
306 to the original activity space before computing reconstruction scores [Low et al., 2018]. A direct
307 analogue for the ODE-VAE is to keep a fixed (or lightly fine-tuned) PCA projection for computational
308 efficiency, but decode back to raw ROI space and compute the main reconstruction loss on $y_b(t) \in \mathbb{R}^N$.
309 One implementation is to parameterize a raw-space decoder as $\hat{y}(t) = W_{\text{PCA}}^\top \hat{x}(t) + \mu$, using the
310 PCA loading matrix W_{PCA} and mean μ from preprocessing, and to define \mathcal{L}_{rec} in raw space. This
311 would more closely match the scientific question—reconstructing neural activity—and reduce the
312 chance that good PCA-space fits hide biologically relevant errors.

313 **10.5 Make latent dynamics probabilistic to better match MIND transition structure**

314 MIND estimates transition structure via a probabilistic model of next-step activity (a PPCA regression
315 forest) and then derives a random-walk geometry from transition probabilities [Low et al., 2018,
316 Tipping and Bishop, 1999, Breiman, 2001]. Our latent ODE is deterministic given $z_{0,b}$, which
317 can be brittle when real data exhibit unmodeled inputs, nonstationarities, or observation noise. A
318 natural extension is to introduce process noise (Neural SDEs) or discrete-time stochastic residuals,
319 $z(t_{\ell+1}) = z(t_\ell) + \int_{t_\ell}^{t_{\ell+1}} f_\theta(z(t), t) dt + \eta_\ell$, which can absorb variability not explained by the initial
320 condition while retaining smooth latent structure. This direction also creates a clearer conceptual
321 bridge between ODE-based dynamics and MIND’s transition-probability graph.

322 **10.6 Geometry-aware objectives beyond soft-LLE**

323 Our current soft-LLE penalty encourages local linearity in the learned latent point cloud, but it
324 does not directly use transition structure. The MIND code constructs local distances from transition
325 probabilities (e.g., $d_{ij} \propto \sqrt{-\log p_{ij}}$) and then computes geodesic distances on the resulting graph
326 before embedding [Low et al., 2018]. This is conceptually related to geodesic-distance embeddings in
327 nonlinear dimensionality reduction [Tenenbaum et al., 2000]. A promising direction is to import this
328 idea as a regularizer: estimate a transition graph among landmarked latent points, compute a random-
329 walk geodesic distance matrix, and penalize distortions between these distances and Euclidean
330 distances in the latent embedding. Such a constraint could encourage the latent representation to
331 respect the sequential structure that MIND leverages, while still permitting an end-to-end generative
332 model.

333 **11 Limitations and Reproducibility**

334 This study is bounded by the available run artifacts and inherits version-specific logging differences.
335 In particular, some run files report “best” and “final” R^2 under different conditions, and not all check-
336 points include identical metadata fields. We therefore report values exactly as saved in each artifact
337 path. The implementation also exhibits training fragility (including occasional NaN divergence),
338 which should be addressed before drawing definitive biological conclusions.

339 **12 Conclusion**

340 We presented a mathematically grounded latent Neural ODE-VAE framework for neural manifold
341 modeling and analyzed a sequence of model variants (v1–v6), with v5 as the primary model. The
342 method can recover smooth low-dimensional dynamics and high synthetic reconstruction quality,
343 but real-data performance remains sensitive to preprocessing and evaluation protocol. This work
344 provides a formal foundation and concrete directions for improving robustness of ODE-VAE manifold
345 modeling for neuroscience.

346 **References**

- 347 Dmitriy Aronov, Rachel Nevers, and David W. Tank. Mapping of a non-spatial dimension by the
348 hippocampal–entorhinal circuit. *Nature*, 543(7647):719–722, 2017.
- 349 Jacob L. S. Bellmund, Peter Gärdenfors, Edvard I. Moser, and Christian F. Doeller. Navigating
350 cognition: Spatial codes for human thinking. *Science*, 362(6415):eaat6766, 2018.
- 351 Leo Breiman. Random forests. *Machine Learning*, 45(1):5–32, 2001.
- 352 Rishidev Chaudhuri, Burak Gerçek, Bikash Pandey, Adrien Peyrache, and Ila Fiete. The intrinsic
353 attractor manifold and population dynamics of a canonical cognitive circuit across waking and
354 sleep. *Nature Neuroscience*, 22:1512–1520, 2019.
- 355 Ricky T. Q. Chen, Yulia Rubanova, Jesse Bettencourt, and David Duvenaud. Neural ordinary
356 differential equations. In *Advances in Neural Information Processing Systems (NeurIPS)*, 2018.
- 357 Alexandra O. Constantinescu, Jill X. O’Reilly, and Timothy E. J. Behrens. Organizing conceptual
358 knowledge in humans with a grid-like code. *Science*, 352(6292):1464–1468, 2016.
- 359 John P. Cunningham and Byron M. Yu. Dimensionality reduction for large-scale neural recordings.
360 *Nature Neuroscience*, 17(11):1500–1509, 2014.
- 361 Howard Eichenbaum and Neal J. Cohen. Can we reconcile the declarative memory and spatial
362 navigation views on hippocampal function? *Neuron*, 83(4):764–770, 2014.
- 363 Howard Eichenbaum, Menachem Kuperstein, Andrew Fagan, and Janet Nagode. Cue-sampling and
364 goal-approach correlates of hippocampal unit activity in rats performing an odor-discrimination
365 task. *Journal of Neuroscience*, 7:716–732, 1987.
- 366 Loren M. Frank, Emery N. Brown, and Matthew Wilson. Trajectory encoding in the hippocampus
367 and entorhinal cortex. *Neuron*, 27:169–178, 2000.
- 368 Juan A. Gallego, Matthew G. Perich, Lee E. Miller, and Sara A. Solla. Neural manifolds for the
369 control of movement. *Neuron*, 94(5):978–984, 2017.
- 370 P. R. Gill, Sheri J. Y. Mizumori, and David M. Smith. Hippocampal episode fields develop with
371 learning. *Hippocampus*, 21:1240–1249, 2011.
- 372 Lauren E. Herzog et al. Interaction of taste and place coding in the hippocampus. *Journal of
373 Neuroscience*, 39:3057–3069, 2019.
- 374 Diederik P. Kingma and Max Welling. Auto-encoding variational bayes. In *International Conference
375 on Learning Representations (ICLR)*, 2014.

- 376 Ryan J. Low, Sean Lewallen, Dmitriy Aronov, Rachel Nevers, and David W. Tank. Probing variability
377 in a cognitive map using manifold inference from neural dynamics. *bioRxiv*, 2018. doi: 10.1101/
378 418939.
- 379 Chris J. MacDonald, Kyle Q. Lepage, Uri T. Eden, and Howard Eichenbaum. Hippocampal “time
380 cells” bridge the gap in memory for discontiguous events. *Neuron*, 71:737–749, 2011.
- 381 Sam McKenzie et al. Hippocampal representation of related and opposing memories develop within
382 distinct, hierarchically organized neural schemas. *Neuron*, 83:202–215, 2014.
- 383 Edward H. Nieh et al. Geometry of abstract learned knowledge in the hippocampus. *Nature*, 595
384 (7865):80–84, 2021.
- 385 John O’Keefe and Jonathan Dostrovsky. The hippocampus as a spatial map. preliminary evidence
386 from unit activity in the freely-moving rat. *Brain Research*, 34(1):171–175, 1971.
- 387 John O’Keefe and Lynn Nadel. *The Hippocampus as a Cognitive Map*. Clarendon Press, 1978.
- 388 Sang Ah Park, David S. Miller, Hamed Nili, Charan Ranganath, and Erie D. Boorman. Map making:
389 Constructing, combining, and inferring on abstract cognitive maps. *Neuron*, 107(6):1226–1238.e8,
390 2020.
- 391 Eva Pastalkova, Vladimir Itskov, A. Amarasingham, and Gyorgy Buzsaki. Internally generated cell
392 assembly sequences in the rat hippocampus. *Science*, 321:1322–1327, 2008.
- 393 Eftychios A. Pnevmatikakis and Andrea Giovannucci. Normcorre: An online algorithm for piecewise
394 rigid motion correction of calcium imaging data. *Journal of Neuroscience Methods*, 291:83–94,
395 2017.
- 396 Eftychios A. Pnevmatikakis et al. Simultaneous denoising, deconvolution, and demixing of calcium
397 imaging data. *Neuron*, 89:285–299, 2016.
- 398 Yulia Rubanova, Ricky T. Q. Chen, and David Duvenaud. Latent ordinary differential equations for
399 irregularly-sampled time series. In *Advances in Neural Information Processing Systems (NeurIPS)*,
400 2019.
- 401 Amir Rubin et al. Revealing neural correlates of behavior without behavioral measurements. *Nature
402 Communications*, 10:1–14, 2019.
- 403 Abigail A. Russo et al. Motor cortex embeds muscle-like commands in an untangled population
404 response. *Neuron*, 97(4):953–966.e8, 2018.
- 405 Lawrence K. Saul and Sam T. Roweis. Think globally, fit locally: Unsupervised learning of low
406 dimensional manifolds. *Journal of Machine Learning Research*, 4:119–155, 2003.
- 407 Nicolas W. Schuck and Yael Niv. Sequential replay of nonspatial task states in the human hippocam-
408 pus. *Science*, 364(6447):eaaw5181, 2019.
- 409 Kimberly L. Stachenfeld, Matthew M. Botvinick, and Samuel J. Gershman. The hippocampus as a
410 predictive map. *Nature Neuroscience*, 20(11):1643–1653, 2017.
- 411 Rita M. Tavares et al. A map for social navigation in the human brain. *Neuron*, 87:231–243, 2015.
- 412 Jiannis Taxidis et al. Differential emergence and stability of sensory and temporal representations in
413 context-specific hippocampal sequences. *Neuron*, 108:984–998.e9, 2020.
- 414 Joshua B. Tenenbaum, Vin de Silva, and John C. Langford. A global geometric framework for
415 nonlinear dimensionality reduction. *Science*, 290(5500):2319–2323, 2000.
- 416 Michael E. Tipping and Christopher M. Bishop. Probabilistic principal component analysis. *Journal
417 of the Royal Statistical Society: Series B*, 61(3):611–622, 1999.
- 418 Edward C. Tolman. Cognitive maps in rats and men. *Psychological Review*, 55(4):189–208, 1948.

419 Eric R. Wood, Paul A. Dudchenko, Rebekka J. Robitsek, and Howard Eichenbaum. Hippocampal
420 neurons encode information about different types of memory episodes occurring in the same
421 location. *Neuron*, 27:623–633, 2000.

422 Byron M. Yu, John P. Cunningham, Gopal Santhanam, Stephen I. Ryu, Krishna V. Shenoy, and
423 Maneesh Sahani. Gaussian-process factor analysis for low-dimensional single-trial analysis of
424 neural population activity. *Journal of Neurophysiology*, 102(1):614–635, 2009.